JACS
JOURNAL OF THE AMERICAN CHEMICAL SOCIETY
Cite This: J. Am. Chem. Soc. XXXX, XXX, XXX−XXX
Communication
pubs.acs.org/JACS

Multifunctional Nanoscale Metal−Organic Layers for Ratiometric pH and Oxygen Sensing

Guangxu Lan,[†,∥] Kaiyuan Ni,[†,∥] Eric You,[†] Maolin Wang,[†,§] August Culbert,[†] Xiaomin Jiang,[†] and Wenbin Lin*[,†,‡]

[†]Department of Chemistry and [‡]Department of Radiation and Cellular Oncology and Ludwig Center for Metastasis Research, The University of Chicago, Chicago, Illinois 60637, United States

[§]College of Chemistry and Molecular Engineering, Peking University, Beijing 100871, China

Supporting Information

ABSTRACT: As a monolayered version of nanoscale metal−organic frameworks (nMOFs), nanoscale metal−organic layers (nMOLs) represent an emerging class of highly tunable two-dimensional materials for hierarchical functionalization and with facile access to analytes. Here we report the design of the first nMOL-based biosensor for ratiometric pH and oxygen sensing in mitochondria. Cationic Hf_{12}-Ru nMOL was solvothermally synthesized by laterally connecting Hf_{12} secondary building units (SBUs) with oxygen-sensitive $Ru(bpy)_3^{2+}$-derived DBB-Ru ligands (bpy = 2,2′-bipyridine). The Hf_{12}-Ru nMOL was then covalently functionalized with pH-sensitive fluorescein isothiocyanate and pH/oxygen-independent Rhodamine-B isothiocyanate through thiourea linkages to afford Hf_{12}-Ru-F/R as a mitochondria-targeted ratiometric sensor for pH and O_2 in live cells. High-resolution confocal microscope imaging with Hf_{12}-Ru-F/R revealed a positive correlation between pH and local O_2 concentration in mitochondria. Our work shows the potential of nMOL-based ratiometric biosensors in sensing and imaging of biologically important analytes in live cells.

The development of biosensors to probe physiological processes and pathobiological factors is of great importance to early disease diagnosis.[1−4] Among many forms of biosensors, optical probes are the most commonly used in cellular sensing and imaging as they permit direct, real-time, and label-free detection of many biological and chemical analytes.[5−10] In particular, nanoparticle-based optical biosensors have afforded powerful tools for minimally invasive analyte monitoring in live cells.[11−17] They provide the foundation to develop multifunctional ratiometric biosensors to precisely monitor a number of biological and chemical factors underlying various pathobiologies.

In the past decade, nanoscale metal−organic frameworks (nMOFs) have shown great potential for biological sensing and related applications.[18−30] By simultaneously incorporating molecular sensors and reference probes as well as ensuring their spatial isolation to avoid self-quenching in the frameworks, nMOFs have provided a novel crystalline molecular nanomaterial platform for designing ratiometric sensors with high sensitivity and resolution.[31,32] However, due to the strict symmetry requirement of bridging ligands and relatively small pores/channels of most nMOFs, only simple molecular sensors can be incorporated into nMOFs and accessible to small analytes, severely limiting the universality of nMOFs in biosensing. We propose that nanoscale metal−organic layers (nMOLs),[33,34] a monolayered version of nMOFs, can overcome these limitations of nMOFs to afford the next generation of two-dimensional nanobiosensors. nMOLs not only retain the molecular nature, structural regularity, and compositional diversity of nMOFs, but also possess high densities of open sites to allow covalent installation of complex molecular sensors and ready access to large analytes. Herein we report the design of a proof-of-concept nMOL-based biosensor, Hf_{12}-Ru-F/R, for ratiometric pH and oxygen sensing in mitochondria (Figure 1).

The Hf_{12}-Ru nMOL was synthesized solvothermally between $HfCl_4$ and $Ru(H_2DBB)(bpy)_2^{2+}$ [H_2DBB-Ru, bpy = 2,2′-bipyridine, DBB = 4,4′-di(4-benzoato)-2,2′-bipyridine] in N,N-dimethylformamide (DMF) at 80 °C with trifluoroacetic acid (TFA) and water as modulators (Figures S1−S3). Hf_{12}-Ru was proposed as an infinite 2D network of **kgd** topology, where Hf_{12} secondary building units (SBUs) were vertically terminated by TFA groups and laterally bridged by DBB-Ru ligands to afford the formula of $Hf_{12}(\mu_3\text{-}O)_8(\mu_3\text{−}OH)_8(\mu_2\text{-}OH)_6(DBB\text{-}Ru)_6(TFA)_6$. The monolayer morphology of Hf_{12}-Ru was demonstrated by transmission electron microscopy (TEM, Figures 2a and S4a) showing a diameter of ∼150 nm and atomic force microscopy (AFM, Figures 2c,d and S4b) giving a thickness of ∼1.7 nm. This thickness is consistent with the modeled height of Hf_{12} clusters capped with TFA groups. Dynamic light scattering (DLS) measurements gave a number-averaged diameter of 98.5 ± 2.2 nm for Hf_{12}-Ru (Figure S9). The proposed topological structure of Hf_{12}-Ru was further confirmed by its similar powder X-ray diffraction (PXRD) pattern to that simulated from a Hf_{12} MOL (Figure 2f)[33] and high-resolution TEM (HRTEM) image along with its fast Fourier transform (FFT, Figure 2b), which revealed a six-fold symmetry and a Hf_{12}−Hf_{12} distance of ∼2.7 nm that matches the modeled structure well. The formulation of Hf_{12}-Ru was further supported by thermogravimetric analysis (Figure S6).

The ratiometric sensor Hf_{12}-Ru-F/R was synthesized by covalently attaching fluorescein isothiocyanate (FITC) and

Received: October 13, 2019
Published: November 20, 2019

DOI: 10.1021/jacs.9b11024
J. Am. Chem. Soc. XXXX, XXX, XXX−XXX

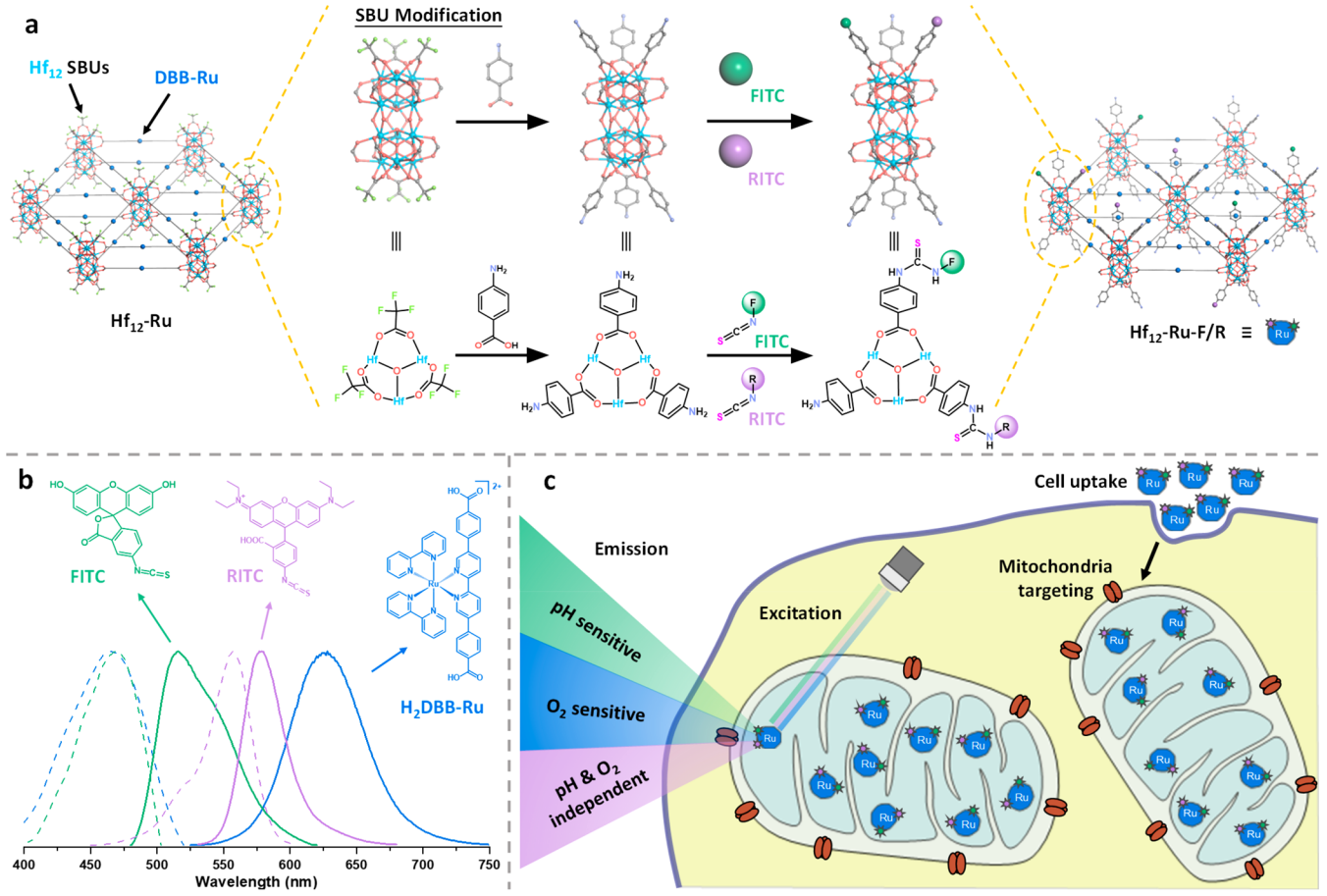

Figure 1. Schematic showing the synthesis of multifunctional Hf_{12}-Ru-F/R. (a) Surface modification of Hf_{12}-Ru by exchanging TFA capping groups on Hf_{12} SBUs with *p*-aminobenzoate groups and covalent conjugation of FITC and RITC to Hf_{12} SBUs by forming thiourea linkages. (b) Chemical structures and excitation/emission spectra of FITC, RITC, and H_2DBB-Ru. (c) Positively charged Hf_{12}-Ru-F/R targets mitochondria and allows ratiometric sensing of intramitochondrial pH and oxygen via the luminescence ratios of pH-sensitive FITC to pH-independent RITC and O_2-sensitive DBB-Ru to O_2-independent RITC, respectively.

rhodamine-B isothiocyanate (RITC) to Hf_{12}-Ru (Figure 1a). Vertically capped TFA groups on Hf_{12} SBUs were first replaced by *p*-aminobenzoate (ABA) to afford Hf_{12}-Ru-ABA with the formula of $Hf_{12}(\mu_3\text{-O})_8(\mu_3\text{-OH})_8(\mu_2\text{-OH})_6(\text{DBB-Ru})_6(\text{ABA})_6$ based on the ^{1}H NMR analysis of digested Hf_{12}-Ru-ABA (Figures S5 and S7). FITC and RITC were then covalently conjugated to ABA-capped Hf_{12} SBUs by forming the ABA-F (between ABA and FITC) and ABA-R (between ABA and RITC) thiourea linkages to generate Hf_{12}-Ru-F/R with the formula of $Hf_{12}(\mu_3\text{-O})_8(\mu_3\text{-OH})_8(\mu_2\text{-OH})_6(\text{DBB-Ru})_6(\text{ABA})_{6\text{-}x\text{-}y}(\text{ABA-F})_x(\text{ABA-R})_y$, where x and y represent FITC and RITC loadings, respectively. The ABA-F and ABA-R moieties in Hf_{12}-Ru-F/R were confirmed by the presence of UV−vis absorptions characteristic of FITC and RITC (Figures 3a and S11−S14) and the observation of $[\text{ABA-F} + \text{H}]^+$ and $[\text{ABA-R}]^+$ peaks in addition to the $[\text{H}_2\text{DBB-Ru}/2]^+$ peaks in the high resolution-mass spectrum (HRMS) of digested Hf_{12}-Ru-F/R (Figure 2g). No signal corresponding to free FITC and RITC was detected, confirming their covalent attachment to the MOL via the thiourea linkages. Compared to Hf_{12}-Ru, Hf_{12}-Ru-F/R displayed similar morphology by TEM (Figures 2e and S8a), identical topological structure by HRTEM (Figure S8b) and PXRD (Figure 2f), and a slightly increased number-averaged size of 119.1 ± 2.3 nm by DLS (Figure S9).

We hypothesized that Hf_{12}-Ru-F/R could allow ratiometric pH sensing based on the fluorescence ratio of pH-sensitive FITC to pH-independent RITC and O_2 sensing based on the luminescence ratio of O_2-sensitive DBB-Ru to O_2-independent RITC. The loadings of FITC and RITC in Hf_{12}-Ru-F/R were optimized to be 1.1 and 5.6 mol%, respectively, to achieve comparable luminescence intensities for FITC, RITC, and DBB-Ru (Figures 3b and S15−S18). Hf_{12}-Ru-F/R with this composition was used in subsequent studies. Calibration curves and *in vitro* sensing studies were performed using excitation/emission wavelengths of 430/620, 465/500, and 535/600 nm for DBB-Ru, FITC, and RITC, respectively (Figure S19). The response of Hf_{12}-Ru-F/R to pH and O_2 was first studied by fluorimetry (Supporting Information (SI), section S3.4). In phosphate buffer solutions (PBS) with pH values of 4.0−8.0 and under normoxia, Hf_{12}-Ru-F/R showed significantly different FITC fluorescence intensities but constant RITC and DBB-Ru signals (Figure 3c). The pH response of Hf_{12}-Ru-F/R is similar to that of free FITC (Figures S20 and S22a) and well fitted with SI eq S1 (R^2 = 0.998, Figure S23). At the same time, Hf_{12}-Ru-F/R showed different DBB-Ru luminescence intensities but constant FITC and RITC signals under varied O_2 partial pressures and a pH of 7.04 (Figure 3d). The O_2 responses of both Hf_{12}-Ru-F/R and H_2DBB-Ru were well fitted to the Stern−Völmer equation (SI eq S5, R^2 = 1, Figure S24) with similar fitting parameters (Figures S21 and S22b). Based on SI eqs S1 and S5, Hf_{12}-Ru-F/R accurately determined the pH and O_2 values of a random

DOI: 10.1021/jacs.9b11024
J. Am. Chem. Soc. XXXX, XXX, XXX−XXX

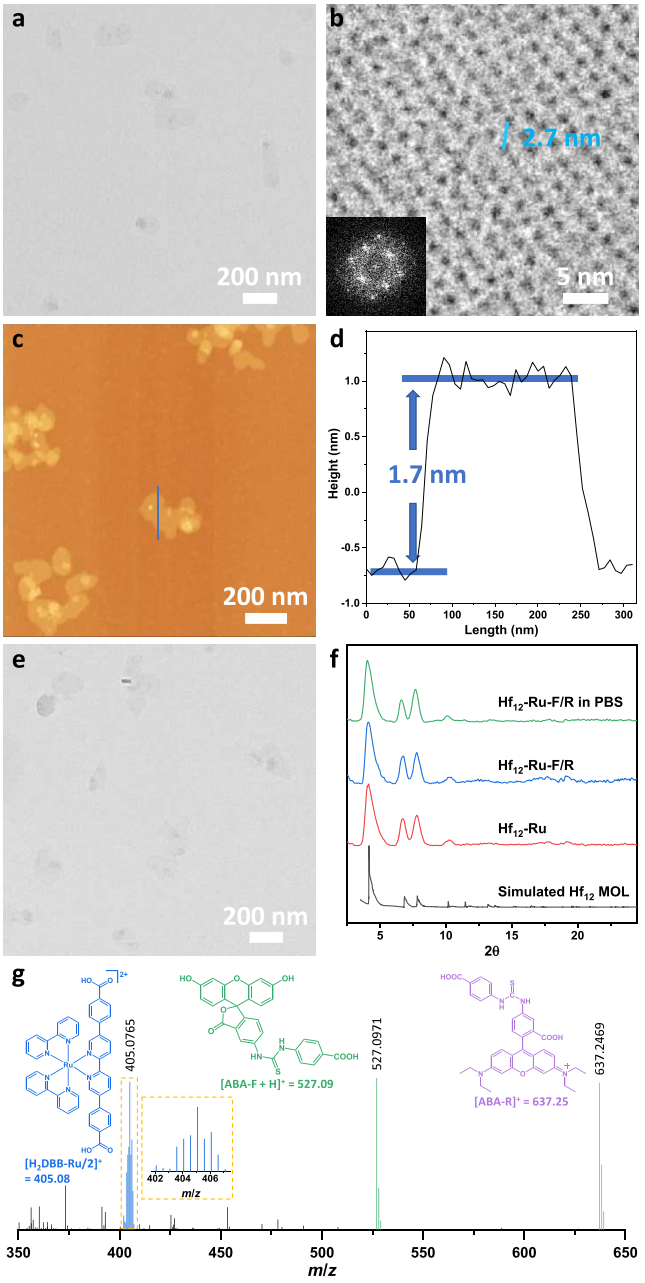

Figure 2. TEM image (a), HRTEM image with the FFT pattern in the inset (b), AFM topography (c) and height profile (d) of Hf_{12}-Ru. (e) TEM image of Hf_{12}-Ru-F/R. (f) PXRD patterns of Hf_{12}-Ru and Hf_{12}-Ru-F/R, freshly prepared or after 4 h incubation in 0.6 mM PBS, in comparison to the simulated pattern for the Hf_{12} MOL. (g) HRMS spectrum of digested Hf_{12}-Ru-F/R.

series of samples (Figure S25). These fluorimetric study results suggest the potential of Hf_{12}-Ru-F/R in ratiometric pH and O_2 sensing.

We next constructed pH and O_2 calibration curves for Hf_{12}-Ru-F/R using an IVIS imaging system. Hf_{12}-Ru-F/R was incubated in PBS at pH values of 4.01, 4.45, 4.99, 5.57, 5.94, 6.46, 7.04, 7.49, and 8.00 under O_2 pressures of 0, 34.1, 63.5, 95.8, 124.2, and 160.0 mmHg) and the luminescence signals of FITC, DBB-Ru, and RITC in Hf_{12}-Ru-F/R were collected separately. As shown in Figure S26, FITC only responded to pH, DBB-Ru only responded to O_2, and RITC did not respond to either pH or O_2. The ratiometric calibration curves for pH

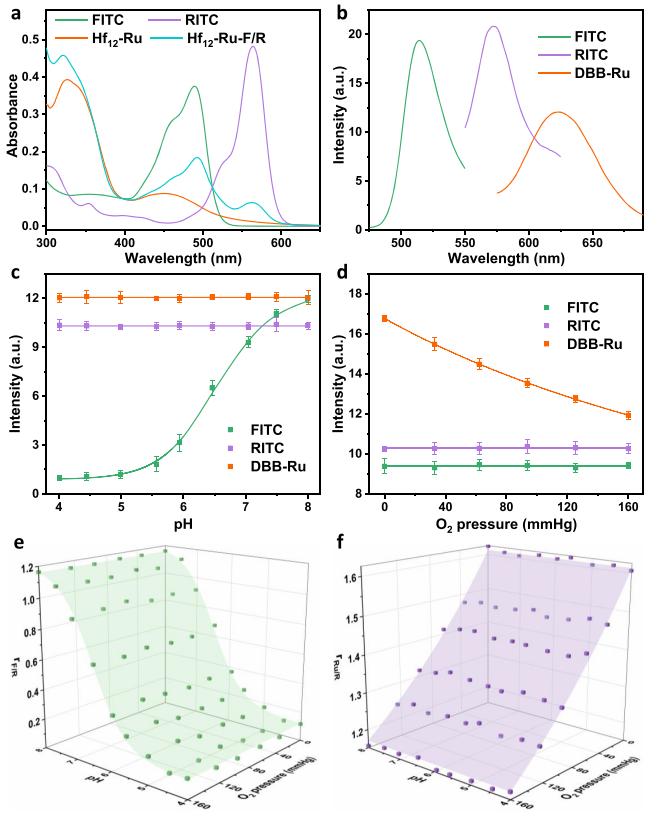

Figure 3. (a) UV−vis spectra of Hf_{12}-Ru and Hf_{12}-Ru-F/R with 31.5 mol% FITC and 10.1 mol% RITC loadings. (b) Luminescence spectra of Hf_{12}-Ru-F/R showing emissions corresponding to FITC, RITC, and DBB-Ru, respectively. Plots of luminescence intensities of Hf_{12}-Ru-F/R at different pHs under normoxia (c) or under different O_2 pressures at pH 7.04 (d), acquired by fluorimetry. Calibration curves for pH (e, eq 1) and O_2 (f, eq 2) of Hf_{12}-Ru-F/R acquired by IVIS imaging. For (b)−(f), the concentration of Hf_{12}-Ru-F/R was 10.0 μM based on DBB-Ru, and Hf_{12}-Ru-F/R had 1.1 mol% FITC and 5.6 mol% RITC loadings.

and O_2 were then established by fitting the dependence of the fluorescence ratio of FITC to RITC ($r_{F/R}$) on pH according to eq 1 (R^2 = 0.996, Figures 3e and S27a) and the dependence of the luminescence ratio of DBB-Ru to RITC ($r_{Ru/R}$) on O_2 pressure (P_{O_2}) according to eq 2 (R^2 = 0.999, Figures 3f and S27b), respectively.

$$r_{F/R} = \frac{0.119e^{-2.303pH} + 3.91 \times 10^{-7}}{e^{-2.303pH} + 3.28 \times 10^{-7}} \quad (1)$$

$$r_{Ru/R} = \frac{1.613}{1 + 0.00237P_{O_2}} \quad (2)$$

The stability of Hf_{12}-Ru-F/R under physiological conditions was demonstrated by the unchanged PXRD pattern after incubation in 0.6 mM PBS for 4 h (Figure 2f). We then evaluated uptake of Hf_{12}-Ru-F/R in mouse colon carcinoma CT26 cells. The highly positive zeta potentials of Hf_{12}-Ru (37.7 ± 1.6 mV) and Hf_{12}-Ru-F/R (26.9 ± 2.2 mV) facilitated their cellular uptake as quantified by ICP-MS (Figure S28). The biocompatibility of Hf_{12}-Ru and Hf_{12}-Ru-F/R was demonstrated by their lack of cytotoxicity in the 3-(4,5-dimethylthiazol-2-yl)-5-(3-carboxymethoxyphenyl)-2-(4-sulfophenyl)-2*H*-tetrazolium assays (Figure S29). We then extracted mitochondria after incubating CT26 cells with

DOI: 10.1021/jacs.9b11024
J. Am. Chem. Soc. XXXX, XXX, XXX−XXX

Hf_{12}-Ru or Hf_{12}-Ru-F/R and determined the percentages of internalized particles in mitochondria by ICP-MS. Both Hf_{12}-Ru and Hf_{12}-Ru-F/R were quickly enriched in mitochondria and reached saturation after 4 h incubation due to their cationic nature (Figure S30). Localization of Hf_{12}-Ru in mitochondria was also visualized by confocal scanning laser microscopy (CLSM).[35] After CT26 cells were incubated with Hf_{12}-Ru for 0, 0.5, 2, and 4 h, CLSM images were captured for colocalization analysis (Figure 4 and S31): 0.5 h post-incubation, enhanced magenta signals of Hf_{12}-Ru were mostly colocalized with red signals representing endo/lysosomes, indicating fast endocytosis of positively charged Hf_{12}-Ru. At the 2 h time point, the majority of Hf_{12}-Ru colocalized with mitochondria, proving its ability to effectively escape from endosomes and simultaneously enrich itself within mitochondria. At the 4 h time point, Hf_{12}-Ru accumulated in mitochondria with no colocalization with endo/lysosomes. CLSM colocalization analysis could not be performed on Hf_{12}-Ru-F/R due to spectral overlap between RITC and Mitotracker Red as well as FITC and Lysotracker Green. These results demonstrate the mitochondria-targeting property of both Hf_{12}-Ru and Hf_{12}-Ru-F/R.

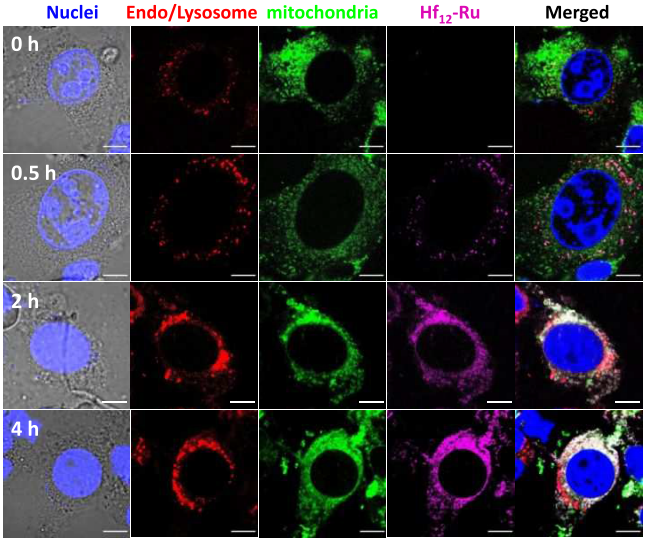

Figure 4. Time-dependent subcellular localization of Hf_{12}-Ru in CT26 cells. Blue, red, green, and magenta colors represent DAPI-stained cell nuclei, endo/lysotracker-stained endo/lysosomes, mitotracker-stained mitochondria, and Hf_{12}-Ru, respectively. Scale bar = 5 μm.

With low background autofluorescence, CT26 cells were used to evaluate the applicability of Hf_{12}-Ru-F/R as a ratiometric sensor in live cells by CLSM. Hf_{12}-Ru-F/R at a concentration of 20 μM based on Hf was incubated with CT26 cells seeded on a 35 mm glass bottom dish for live cell imaging. After removing the supernatant and refilling with air, N_2/air mixture, and N_2 to mimic normoxic, hypoxic, and anoxic conditions, respectively, dishes were sealed tightly and scanned under a confocal microscope with different objective lens. At both low (Figure S32) and high (Figure 5a) magnifications, cells under anoxic conditions presented bright magenta signals of DBB-Ru and dim green signals of FITC, consistent with low P_{O_2} and pH values. In contrast, under normoxic conditions, cells showed high FITC signals and low DBB-Ru signals, consistent with high P_{O_2} and pH values. We randomly picked regions of interest (ROIs) in each high-resolution CLSM image (Figure S33) to obtain intensity readouts from ImageJ. The calculated $r_{F/R}$ is inversely proportional to $r_{Ru/R}$ (Figure S34). We repeated imaging studies under normoxic conditions to show the robustness and reproducibility of our ratiometric sensing system (Figure S35). Analysis of over 300 ROIs showed a positive correlation between pH and local O_2 concentration inside mitochondria (Figure 5b). This conclusion matches the previously qualitative studies.[36,37] Our work presents the first quantitative study to establish the correlation between pH and O_2 in mitochondria.

In summary, we have demonstrated the first biological sensing using multifunctional nMOLs. Covalent conjugation of FITC and RITC on the surface of the Hf_{12}-Ru MOL afforded Hf_{12}-Ru-F/R as a mitochondria-targeted ratiometric sensor for real-time monitoring of pH and O_2 in live cells. High-resolution confocal microscope imaging using Hf_{12}-Ru-F/R as a ratiometric sensor provided the first quantitative evidence for a positive correlation between pH and local O_2 concentration in mitochondria. This study establishes the potential of nMOL-based ratiometric biosensors in sensing and imaging

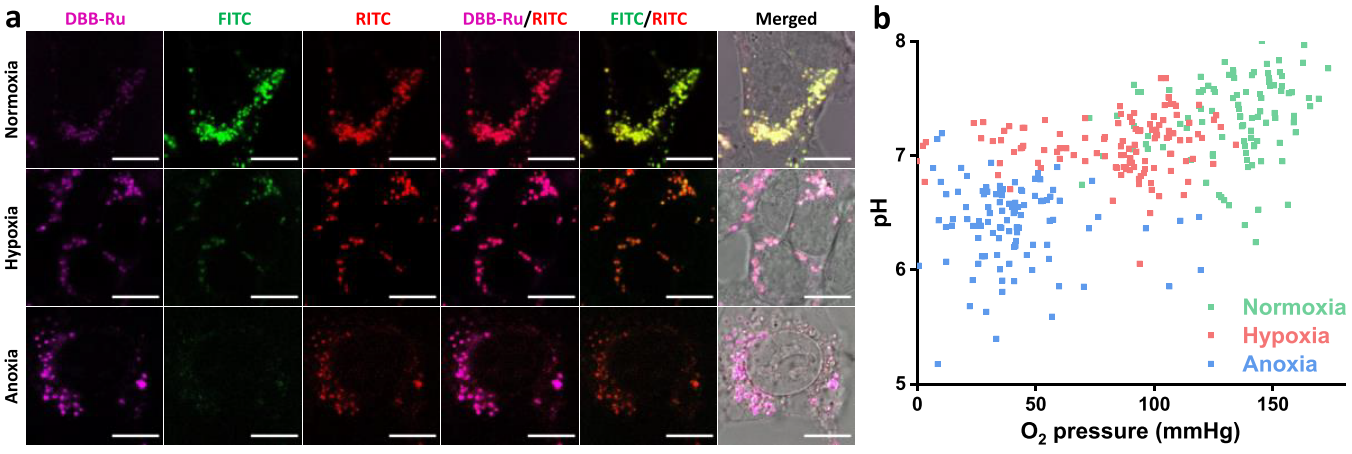

Figure 5. (a) Ratiometric luminescence imaging of CT26 cells after incubation with Hf_{12}-Ru-F/R under normoxia, hypoxia, and anoxia conditions. Scale bar = 10 μm. (b) Scatter plot showing a positive correlation between pH and P_{O_2} in mitochondria as sensed by Hf_{12}-Ru-F/R. Statistical analysis gave a Pearson correlation coefficient (r) of 0.66.

DOI: 10.1021/jacs.9b11024
J. Am. Chem. Soc. XXXX, XXX, XXX−XXX

of biologically important analytes in order to reveal new insights into physiological processes in live cells.

■ ASSOCIATED CONTENT

Supporting Information

The Supporting Information is available free of charge at https://pubs.acs.org/doi/10.1021/jacs.9b11024.

Synthesis and characterization of Hf_{12}-Ru and Hf_{12}-Ru-F/R, luminescence analysis, and in vitro pH and O_2 sensing, including Figures S1−S35 (PDF)

■ AUTHOR INFORMATION

Corresponding Author

*wenbinlin@uchicago.edu

ORCID

Guangxu Lan: 0000-0002-0415-5849
Kaiyuan Ni: 0000-0002-8152-6746
Xiaomin Jiang: 0000-0001-8304-4938
Wenbin Lin: 0000-0001-7035-7759

Author Contributions

‖G.L. and K.N. contributed equally.

Notes

The authors declare no competing financial interest.

■ ACKNOWLEDGMENTS

We thank Dr. Nining Guo and Samuel Veroneau for experimental help. We thank the National Cancer Institute (U01-CA198989 and 1R01CA216436), the University of Chicago Medicine Comprehensive Cancer Center (NIH CCSG: P30 CA014599), and the Ludwig Institute for Metastasis Research for funding support.

■ REFERENCES

(1) Casey, J. R.; Grinstein, S.; Orlowski, J. Sensors and regulators of intracellular pH. *Nat. Rev. Mol. Cell Biol.* **2010**, *11* (1), 50−61.

(2) Webb, B. A.; Chimenti, M.; Jacobson, M. P.; Barber, D. L. Dysregulated pH: a perfect storm for cancer progression. *Nat. Rev. Cancer* **2011**, *11* (9), 671−677.

(3) Harris, A. L. Hypoxia — a key regulatory factor in tumour growth. *Nat. Rev. Cancer* **2002**, *2*, 38.

(4) Yu, M.; Xu, J.; Zheng, J. Renal Clearable Luminescent Gold Nanoparticles: From the Bench to the Clinic. *Angew. Chem.* **2019**, *131* (13), 4156−4172.

(5) Clark, H. A.; Hoyer, M.; Philbert, M. A.; Kopelman, R. Optical Nanosensors for Chemical Analysis inside Single Living Cells. 1. Fabrication, Characterization, and Methods for Intracellular Delivery of PEBBLE Sensors. *Anal. Chem.* **1999**, *71* (21), 4831−4836.

(6) Benjaminsen, R. V.; Sun, H.; Henriksen, J. R.; Christensen, N. M.; Almdal, K.; Andresen, T. L. Evaluating Nanoparticle Sensor Design for Intracellular pH Measurements. *ACS Nano* **2011**, *5* (7), 5864−5873.

(7) Cooper, M. A. Optical biosensors in drug discovery. *Nat. Rev. Drug Discovery* **2002**, *1* (7), 515−528.

(8) Chung, C. Y.-S.; Posimo, J. M.; Lee, S.; Tsang, T.; Davis, J. M.; Brady, D. C.; Chang, C. J. Activity-based ratiometric FRET probe reveals oncogene-driven changes in labile copper pools induced by altered glutathione metabolism. *Proc. Natl. Acad. Sci. U. S. A.* **2019**, *116* (37), 18285.

(9) Gao, P.; Pan, W.; Li, N.; Tang, B. Fluorescent probes for organelle-targeted bioactive species imaging. *Chemical Science* **2019**, *10* (24), 6035−6071.

(10) Wan, X.; Zhang, X.; Pan, W.; Liu, B.; Yu, L.; Wang, H.; Li, N.; Tang, B. Ratiometric Fluorescent Quantification of the Size-Dependent Cellular Toxicity of Silica Nanoparticles. *Anal. Chem.* **2019**, *91* (9), 6088−6096.

(11) Buck, S. M.; Xu, H.; Brasuel, M.; Philbert, M. A.; Kopelman, R. Nanoscale probes encapsulated by biologically localized embedding (PEBBLEs) for ion sensing and imaging in live cells. *Talanta* **2004**, *63* (1), 41−59.

(12) Koo, Y.-E. L.; Cao, Y.; Kopelman, R.; Koo, S. M.; Brasuel, M.; Philbert, M. A. Real-Time Measurements of Dissolved Oxygen Inside Live Cells by Organically Modified Silicate Fluorescent Nanosensors. *Anal. Chem.* **2004**, *76* (9), 2498−2505.

(13) Wu, C.; Bull, B.; Christensen, K.; McNeill, J. Ratiometric Single-Nanoparticle Oxygen Sensors for Biological Imaging. *Angew. Chem., Int. Ed.* **2009**, *48* (15), 2741−2745.

(14) Zhao, Q.; Zhou, X.; Cao, T.; Zhang, K. Y.; Yang, L.; Liu, S.; Liang, H.; Yang, H.; Li, F.; Huang, W. Fluorescent/phosphorescent dual-emissive conjugated polymer dots for hypoxia bioimaging. *Chemical Science* **2015**, *6* (3), 1825−1831.

(15) Chojnacki, P.; Mistlberger, G.; Klimant, I. Separable Magnetic Sensors for the Optical Determination of Oxygen. *Angew. Chem., Int. Ed.* **2007**, *46* (46), 8850−8853.

(16) Chen, S.; Hong, Y.; Liu, Y.; Liu, J.; Leung, C. W. T.; Li, M.; Kwok, R. T. K.; Zhao, E.; Lam, J. W. Y.; Yu, Y.; Tang, B. Z. Full-Range Intracellular pH Sensing by an Aggregation-Induced Emission-Active Two-Channel Ratiometric Fluorogen. *J. Am. Chem. Soc.* **2013**, *135* (13), 4926−4929.

(17) Medintz, I. L.; Stewart, M. H.; Trammell, S. A.; Susumu, K.; Delehanty, J. B.; Mei, B. C.; Melinger, J. S.; Blanco-Canosa, J. B.; Dawson, P. E.; Mattoussi, H. Quantum-dot/dopamine bioconjugates function as redox coupled assemblies for in vitro and intracellular pH sensing. *Nat. Mater.* **2010**, *9* (8), 676−684.

(18) Furukawa, H.; Cordova, K. E.; O'Keeffe, M.; Yaghi, O. M. The Chemistry and Applications of Metal-Organic Frameworks. *Science* **2013**, *341* (6149), 1230444.

(19) Kreno, L. E.; Leong, K.; Farha, O. K.; Allendorf, M.; Van Duyne, R. P.; Hupp, J. T. Metal−Organic Framework Materials as Chemical Sensors. *Chem. Rev.* **2012**, *112* (2), 1105−1125.

(20) Hu, Z.; Deibert, B. J.; Li, J. Luminescent metal−organic frameworks for chemical sensing and explosive detection. *Chem. Soc. Rev.* **2014**, *43* (16), 5815−5840.

(21) Cui, Y.; Yue, Y.; Qian, G.; Chen, B. Luminescent Functional Metal−Organic Frameworks. *Chem. Rev.* **2012**, *112* (2), 1126−1162.

(22) Wu, P.; Wang, J.; He, C.; Zhang, X.; Wang, Y.; Liu, T.; Duan, C. Luminescent Metal-Organic Frameworks for Selectively Sensing Nitric Oxide in an Aqueous Solution and in Living Cells. *Adv. Funct. Mater.* **2012**, *22* (8), 1698−1703.

(23) Foucault-Collet, A.; Gogick, K. A.; White, K. A.; Villette, S.; Pallier, A.; Collet, G.; Kieda, C.; Li, T.; Geib, S. J.; Rosi, N. L.; Petoud, S. Lanthanide near infrared imaging in living cells with Yb^{3+} nano metal organic frameworks. *Proc. Natl. Acad. Sci. U. S. A.* **2013**, *110* (43), 17199.

(24) Rabone, J.; Yue, Y. F.; Chong, S. Y.; Stylianou, K. C.; Bacsa, J.; Bradshaw, D.; Darling, G. R.; Berry, N. G.; Khimyak, Y. Z.; Ganin, A. Y.; Wiper, P.; Claridge, J. B.; Rosseinsky, M. J. An Adaptable Peptide-Based Porous Material. *Science* **2010**, *329* (5995), 1053.

(25) Morris, W.; Briley, W. E.; Auyeung, E.; Cabezas, M. D.; Mirkin, C. A. Nucleic Acid−Metal Organic Framework (MOF) Nanoparticle Conjugates. *J. Am. Chem. Soc.* **2014**, *136* (20), 7261−7264.

(26) Levine, D. J.; Runčevski, T.; Kapelewski, M. T.; Keitz, B. K.; Oktawiec, J.; Reed, D. A.; Mason, J. A.; Jiang, H. Z. H.; Colwell, K. A.; Legendre, C. M.; FitzGerald, S. A.; Long, J. R. Olsalazine-Based Metal−Organic Frameworks as Biocompatible Platforms for H2 Adsorption and Drug Delivery. *J. Am. Chem. Soc.* **2016**, *138* (32), 10143−10150.

(27) Zeng, J.-Y.; Zou, M.-Z.; Zhang, M.; Wang, X.-S.; Zeng, X.; Cong, H.; Zhang, X.-Z. π-Extended Benzoporphyrin-Based Metal−Organic Framework for Inhibition of Tumor Metastasis. *ACS Nano* **2018**, *12* (5), 4630−4640.

DOI: 10.1021/jacs.9b11024
J. Am. Chem. Soc. XXXX, XXX, XXX−XXX

(28) Zheng, X.; Wang, L.; Pei, Q.; He, S.; Liu, S.; Xie, Z. Metal−Organic Framework@Porous Organic Polymer Nanocomposite for Photodynamic Therapy. *Chem. Mater.* **2017**, *29* (5), 2374−2381.
(29) Park, J.; Jiang, Q.; Feng, D.; Mao, L.; Zhou, H.-C. Size-Controlled Synthesis of Porphyrinic Metal−Organic Framework and Functionalization for Targeted Photodynamic Therapy. *J. Am. Chem. Soc.* **2016**, *138* (10), 3518−3525.
(30) Lan, G.; Ni, K.; Lin, W. Nanoscale metal−organic frameworks for phototherapy of cancer. *Coord. Chem. Rev.* **2019**, *379*, 65−81.
(31) Xu, R.; Wang, Y.; Duan, X.; Lu, K.; Micheroni, D.; Hu, A.; Lin, W. Nanoscale Metal−Organic Frameworks for Ratiometric Oxygen Sensing in Live Cells. *J. Am. Chem. Soc.* **2016**, *138* (7), 2158−2161.
(32) He, C.; Lu, K.; Lin, W. Nanoscale Metal−Organic Frameworks for Real-Time Intracellular pH Sensing in Live Cells. *J. Am. Chem. Soc.* **2014**, *136* (35), 12253−12256.
(33) Lan, G.; Ni, K.; Veroneau, S. S.; Song, Y.; Lin, W. Nanoscale Metal−Organic Layers for Radiotherapy−Radiodynamic Therapy. *J. Am. Chem. Soc.* **2018**, *140* (49), 16971−16975.
(34) Lan, G.; Quan, Y.; Wang, M.; Nash, G. T.; You, E.; Song, Y.; Veroneau, S. S.; Jiang, X.; Lin, W. Metal−Organic Layers as Multifunctional Two-Dimensional Nanomaterials for Enhanced Photoredox Catalysis. *J. Am. Chem. Soc.* **2019**, *141* (40), 15767−15772.
(35) Ni, K.; Lan, G.; Veroneau, S. S.; Duan, X.; Song, Y.; Lin, W. Nanoscale metal-organic frameworks for mitochondria-targeted radiotherapy-radiodynamic therapy. *Nat. Commun.* **2018**, *9* (1), 4321.
(36) Chacon, E.; Reece, J. M.; Nieminen, A. L.; Zahrebelski, G.; Herman, B.; Lemasters, J. J. Distribution of electrical potential, pH, free Ca2+, and volume inside cultured adult rabbit cardiac myocytes during chemical hypoxia: a multiparameter digitized confocal microscopic study. *Biophys. J.* **1994**, *66* (4), 942−952.
(37) Solaini, G.; Baracca, A.; Lenaz, G.; Sgarbi, G. Hypoxia and mitochondrial oxidative metabolism. *Biochim. Biophys. Acta, Bioenerg.* **2010**, *1797* (6), 1171−1177.

DOI: 10.1021/jacs.9b11024
J. Am. Chem. Soc. XXXX, XXX, XXX−XXX